PROCEEDINGS, 50th Workshop on Geothermal Reservoir Engineering
Stanford University, Stanford, California, February 10-12, 2025
SGP-TR-229

DAS moment tensor inversion analysis for microseismic events observed during the 2023 circulation tests at Utah FORGE

Ismael Vera Rodriguez[1], Thomas Coleman[1], David Podrasky[1], Carlos Maldaner[1], Yuanyuan Ma[2], Jonathan Ajo-Franklin[2], and the FOGMORE@FORGE Team

[1] Silixa, Environment & Infrastructure, Missoula, Montana

[2] Rice University, Earth, Environmental and Planetary Sciences, Houston, Texas

Ismael.Vera.Rodriguez@lunainc.com

Keywords: Fiber optic sensing, microseismic, moment tensor inversion, DAS, Utah FORGE

ABSTRACT

We analyzed moment tensor resolvability for microseismic events recorded with two distributed acoustic sensing (DAS) systems deployed at the Frontier Observatory for Research in Geothermal Energy or Utah FORGE. The seismicity was observed during circulation tests conducted in July 2023 to evaluate the hydraulic connectivity between two lateral wells, an injector well [16A(78)-32] and a production well [16B(78)-32]. Our analysis of condition numbers indicates that a full moment tensor inversion is not well constrained using only the borehole DAS arrays. Nevertheless, after running a bootstrap analysis, we observed that most of the sensitivity is concentrated in the strike and rake of the dislocation angles derived from the moment tensor solutions. The dip and the angle alpha (i.e., deviation from the pure double-couple case) show more consistency. Analysis of the best constrained moment tensor solutions shows microseismicity that activated in oblique-normal and strike-slip mode with predominantly opening angles around 30° and less. The opening component is consistent with stimulation from the hydraulic injection. We expect that microseismic source mechanisms can inform models of fracture distribution and connectivity important to characterize and to understand the performance of the Enhanced Geothermal System at FORGE. For more recent stimulation work at the site, the availability of a third DAS array in a deep vertical well and a dense surface array of geophones can likely be exploited to estimate fully constrained moment tensor solutions.

1. INTRODUCTION

The Frontier Observatory for Research in Geothermal Energy (FORGE) is an underground laboratory sponsored by the US Department of Energy. The laboratory is a test bed that institutions use for advancing research in Enhanced Geothermal Systems. Utah FORGE is located southwest of Salt Lake City near the town of Milford. The geothermal reservoir is located inside a granitoid formation that presents a westward dipping contact with overlying sedimentary layers (Jones et al., 2024). In July 2023, circulation tests were conducted at FORGE to investigate hydraulic connection between the injector well 16A(78)-32 hydraulically fractured in April 2022, and the production well 16B(78)-32 drilled about a year later in April-July 2023 (Figure 1).

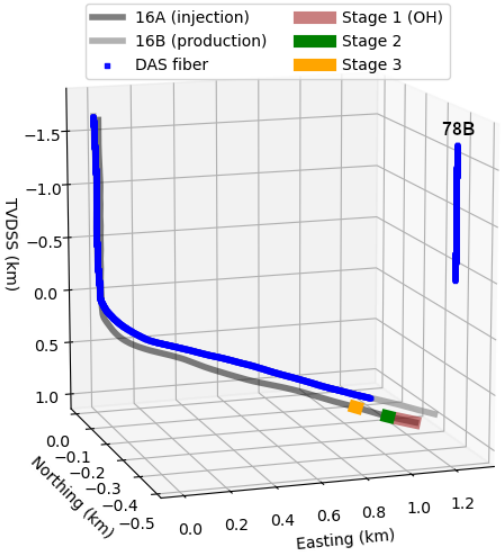

Figure 1: Schematics of the DAS microseismic monitoring geometry during the 2023 circulation tests at Utah FORGE.

Part of the circulation tests were monitored using DAS cables deployed behind casing in the production well (16B) and an additional vertical monitoring well, 78B-32 (see Figure 1). A multimode fiber in well 16B was interrogated with a Silixa iDAS™ v3 unit at a sampling rate of 0.1 ms and a gauge length of 10 m. The total number of channels recorded in this well was 3,264 at spacings of approximately 1 m. As a result of manufacturing difficulties with the cable, a higher than usual noise floor was observed in this well. A singlemode fiber in well 78B was interrogated using a Silixa iDAS v2 system with the same gauge length and approximate channel spacing as in well 16B, albeit with a lower sampling rate of 1 ms. The total number of channels in this well was 1,344. In both cases, the fibers were cemented behind the casing within a ¼" OD steel tube cable construction.

The circulation tests were conducted in two phases. The first stage took place during the early days of July, 2023; this was before the casing and DAS fiber were installed in the production well 16B. Thus, it was for the second phase that both DAS systems could be used to monitor the microseismicity associated with the circulation tests. The injection in the second phase started in well 16A at about 18:00 UTC on July 18 and lasted for a couple of days.

2. METHODS

2.1 Real time event detection

Event detection was conducted in real time using a method based on root-mean-square (RMS) stacks. The methodology exploits the spatial data-density native to DAS. It also shows higher success rate compared to short-term-average over long-term-average (STA/LTA) ratios in terms of number of detections and reduction of false triggers. Before converting to RMS domain, the data is preconditioned with filters that include band-pass and common mode noise (CMN) denoising. Once in RMS domain the data from multiple wells can be combined to generate a joint detection function. In multi-well scenarios like Utah FORGE where the fibers are interrogated with independent DAS units, the combination of RMS-panels provides additional attenuation of both random noise and coherent noise that is not in phase in different wells (e.g., common mode noise). In this case, however, the bandwidth connection between wells 16B and 78B was not enough to allow real-time access to the data recorded from both wells, therefore, the trigger detection was carried on using only the data stream from well 16B. Figure 2 presents examples of events detected using this methodology.

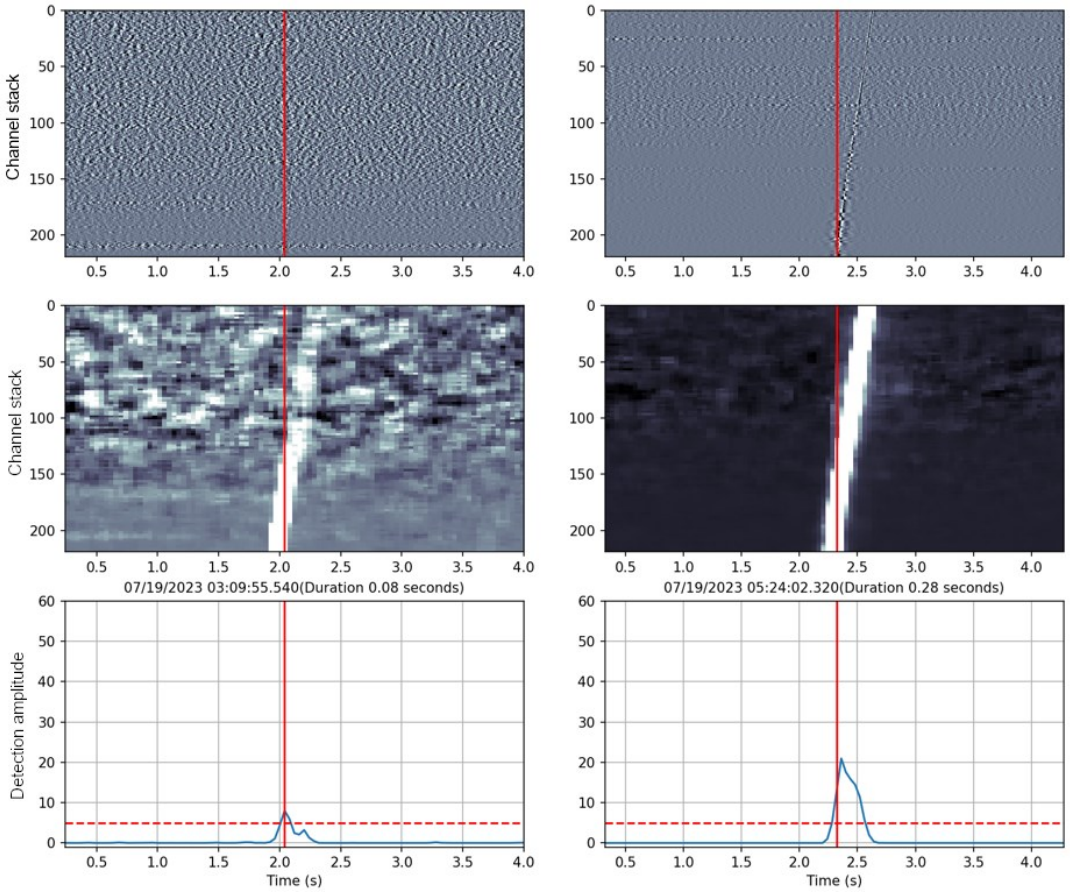

Figure 2: Examples of one weak (left) and one strong (right) detection observed during the second phase of the 2023 circulation tests at Utah FORGE. Top panels are time domain data, middle panels the preconditioned data converted to RMS domain, and bottom panels the derived detection functions. Vertical red lines are trigger times and horizontal dashed lines the detection threshold.

2.2 Joint event location and 3D velocity model inversion

In earlier work, we performed a joint event location and 1D velocity model inversion using a subset of 5 microseismic events detected during the 2023 circulation tests (Vera Rodriguez et al., 2024). Using that model, we estimated the locations of the detected microseismicity through a relative location method. More recently in April 2024, we monitored microseismic activity associated with new stimulation work conducted in wells 16A and 16B. For this monitoring, we had access to a third DAS system deployed in a vertical offset well operated by Fervo Energy (i.e., Delano). Delano is a deep vertical monitoring well located southwest of the pair 16A/16B at a distance of about 1.2 km. Thus, using a subset of 45 microseismic events detected at the three wells, we repeated the joint location and velocity model inversion process. In this new inversion the velocity model was parametrized in 3D, with each layer defined by the velocities of compressional and shear waves, its depth, a dip, and a dipping azimuth. As in our previous work, the inversion algorithm was a heuristic optimizer largely based on particle swarm optimization (Vera Rodriguez, 2019).

2.3 Relative event location

The location results using the originally inverted 1D model arranged into three features that could be correlated with the three stages previously stimulated in well 16A (Vera Rodriguez et al., 2024). However, those results were inconsistent with relative locations estimated independently using near-surface seismic-station data with a 3D model (Niemz et al., 2024). Therefore, we repeated the event location process using our new inverted 3D model. As in our first results, we used a relative location method. In this method, the absolute locations of a subset of events are estimated using time picks. These events become anchors to locate the rest of the microseismic detections. To estimate the relative location of an event we first cross-correlate it with all the anchor events. The anchor event with the highest cross-correlation is then used as the reference for the relative location. For the actual location, the traces from the anchor and the event to be located are cross-correlated to generate correlation gathers, these gathers are then corrected in their moveout using differential times of P- and S-wave arrivals computed in a grid centered around the absolute location of the anchor. The grid node that maximizes the combined stack of P- and S-waves after moveout correction is finally selected as the relative location. Further details about the methodology can be found in Shashidar et al. (2020).

2.4 DAS full moment tensor inversion

Waveform matching full moment tensor inversion was performed with distributed strain wavefields (Vera Rodriguez and Wuestefeld, 2020). The far-field displacement of a point source in terms of its moment tensor is represented as

$$u(\mathbf{x}) = \sum_{i=1}^{i=6} G_i(\mathbf{x}) m_i \tag{1}$$

where G_i are Green's functions convolved with a source time function, and m_i are the corresponding moment tensor coefficients (i.e., xx, xy, xz, yy, yz and zz). Without losing generality, we can consider that Equation 1 represents only the component of the displacement field that is tangential to a DAS fiber. The DAS response for a straight fiber can be represented with

$$d(\mathbf{x}) = \frac{1}{GL}\int_{\mathbf{x}-0.5GL}^{\mathbf{x}+0.5GL} \frac{\partial u}{\partial \hat{x}_t} d\hat{x}_t = \frac{1}{GL}[u(\mathbf{x}+0.5GL) - u(\mathbf{x}-0.5GL)] \tag{2}$$

where GL is the gauge length, $\hat{x}_t$ a unit vector in the direction tangential to the fiber, and $\mathbf{x}$ the DAS channel location. Thus, by substituting Equation 1 in Equation 2, we can have far-field DAS measurements represented in terms of the source moment tensor as

$$d(\mathbf{x}) = \frac{1}{GL}\sum_{i=1}^{i=6}\int_{\mathbf{x}-0.5GL}^{\mathbf{x}+0.5GL} \frac{\partial}{\partial x_t} G_i(\mathbf{x}) m_i dx_t = \frac{1}{GL}\sum_{i=1}^{i=6}[G_i(\mathbf{x}+0.5GL) - G_i(\mathbf{x}-0.5GL)]\, m_i \tag{3}$$

For the moment tensor inversion we used the new 3D velocity model to compute the required Green's functions. For the source time function we utilized a Brune model (Brune, 1970). The corner frequency was one of the parameters optimized by the inversion. Other optimized variables include station corrections independently estimated for P- and S-arrivals to maximize the waveform alignment between observed and modeled data. The workflow is similar to that presented by Vera Rodriguez et al. (2018). The preprocessing consisted of transforming the raw DAS data to strain units, applying CMN denoising, a band pass filter in the 5-120 Hz frequency range, and detrending. The data that input the inversion consisted of the DAS records from both 78B and 16B wells, although the bottom channels in well 16B were removed to minimize bias introduced by the inclusion of near-field data. Arrivals from both wells with signal-to-noise ratios (SNR) below 2 were discarded. The SNR was computed with

$$SNR = \frac{rms(arrival\ window)}{rms(noise\ window)} \tag{4}$$

where the noise window was specified before the direct P-arrival for both P and S SNR computations. A bootstrap analysis was conducted after corner frequency and station corrections were optimized. This analysis utilized 100 random realizations each including 80% of the SNR filtered observations. The output of the bootstrap analysis were mean and standard deviations for inverted moment tensors, derived dislocation angles, solution misfit, and condition number of the sensitivity matrix inverted to estimate a solution. Dislocation angles were derived using a biaxial decomposition of the moment tensors (Chapman and Leaney, 2012). The biaxial decomposition is a general model that includes non-double couple dislocations; these are important to consider in applications of fluid injections.

3. RESULTS

In total, 257 events were detected using our triggering approach, although some of them correspond to more than one closely spaced events detected within the same time window. When plotted together with the pressure at the wellhead of injection well 16A we observe that there is a delayed seismogenic response of about 7.5 hours between the start of pressure build up and the start of event detections (Figure 3). This behavior is visible during the two cycles of pressure increase/decrease that we could monitor. The delay is shortened to about 3 hours during the second cycle.

Despite its simplicity, the new 3D velocity model is more consistent (compared to our initial 1D model) with what is currently known about the structural geology in the area (Figure 4). It has the advantage that the seismic sources were located inside the granitoid reservoir, so that structures internal to the granitoid body could be at least roughly resolved by the inversion. In contrast, these internal details can be invisible to surface source-receiver pairs due to the strong reflectivity of the granitoid contact with the overlying sedimentary layers.

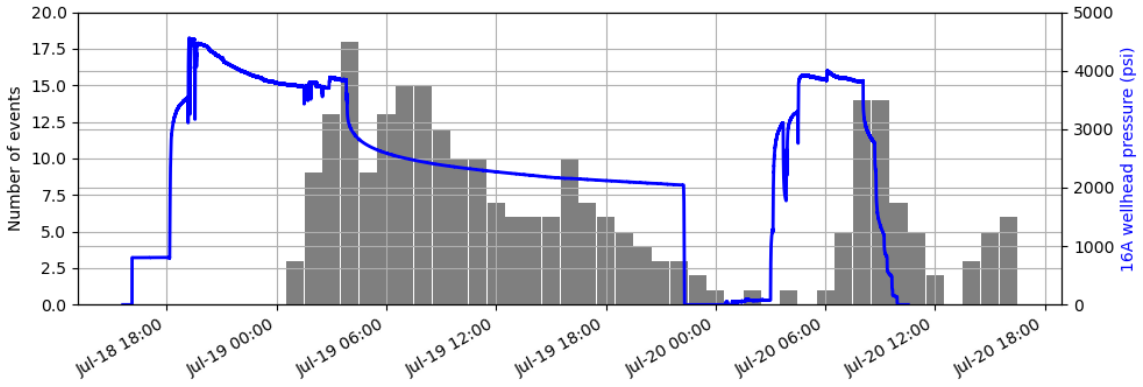

Figure 3: Correlation between the rate of event detections using DAS and wellhead pressure at well 16A. Times are UTC, July 2023.

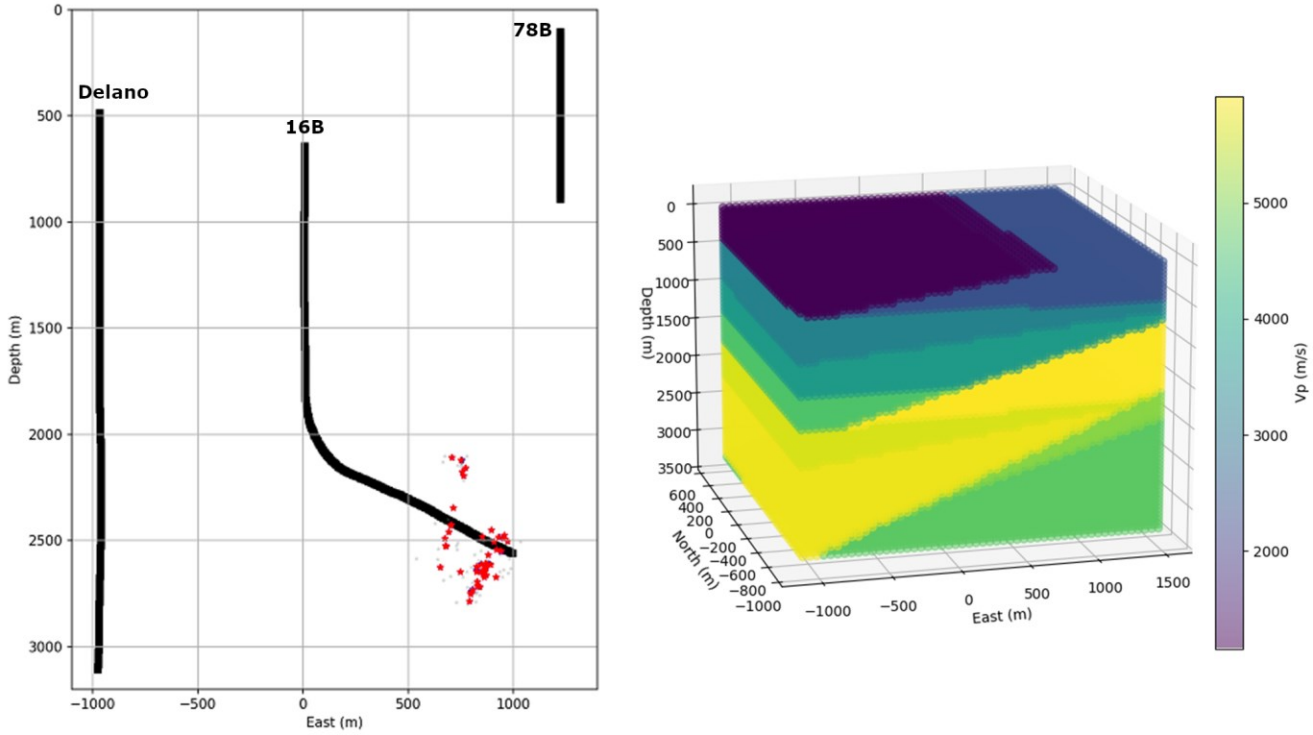

Figure 4: Results from the joint location (left panel) and 3D velocity model (right panel, only P-velocity volume shown) inversion using 45 events detected at three DAS-instrumented wells during the 2024 stimulation campaign. Black lines cover only sections of the wells with the DAS channels used in this inversion.

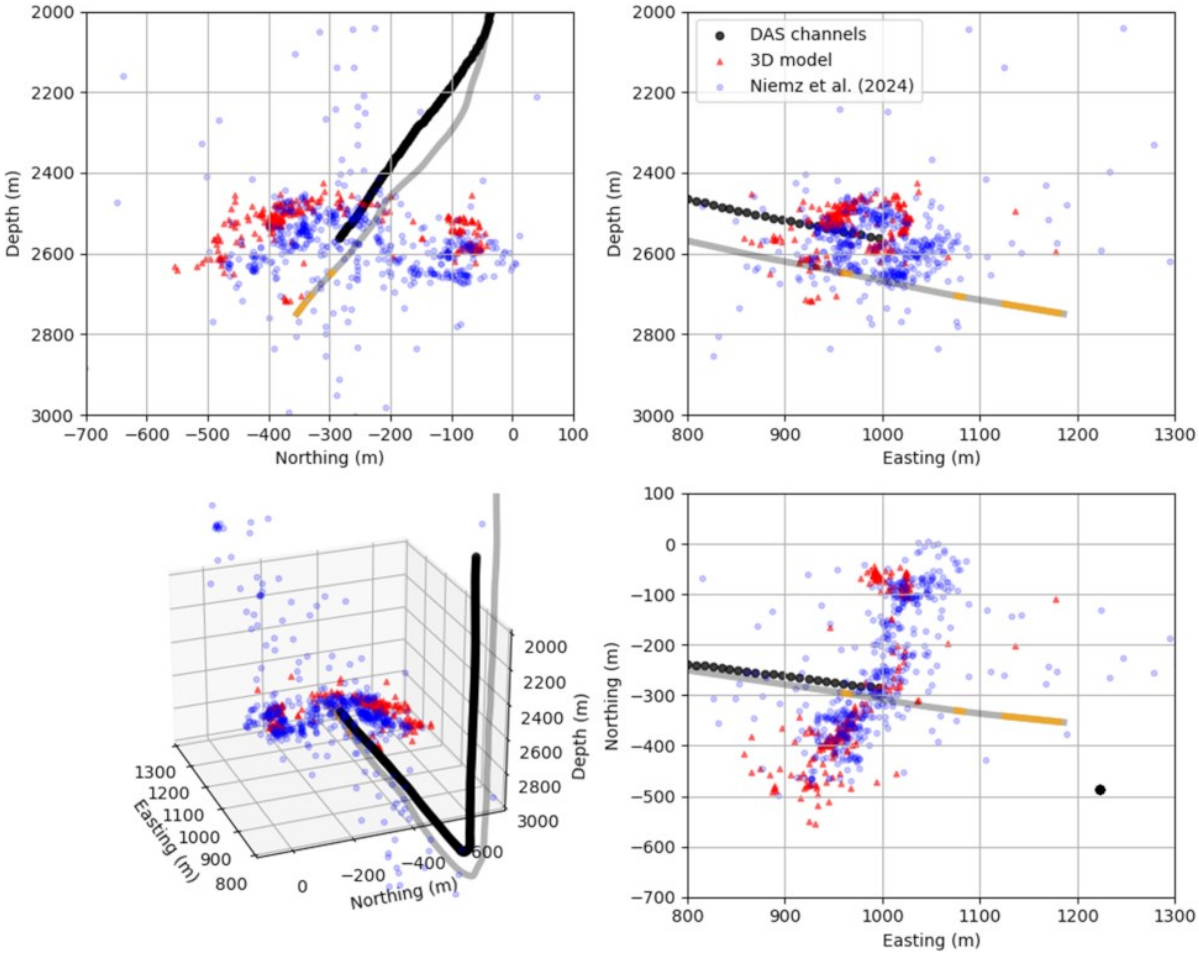

Figure 5: Comparison of location results using DAS data with the new 3D model (red triangles) and independent locations estimated with near-surface seismic stations (blue circles) for the 2023 circulation tests.

The relative location results using the new 3D model are also more consistent with independent locations estimated with near-surface seismic stations (Niemz et al., 2024). The new results cluster forming two main concentrations that seem to be connected. These concentrations can be more directly correlated to the third stage stimulated in well 16A in 2022 (Figure 5).

Condition numbers associated with the moment tensor inversion display higher values near the trajectories of the 16A/16B wells. This is understandable as the trajectory of the vertical monitoring well 78B falls near the vertical plane that contains the geometry of the other monitoring well, i.e., 16B. This reduces focal coverage to constrain a full moment tensor solution (Vera Rodriguez and Wuestefeld, 2020). Condition numbers in the 100s can nevertheless be observed for the events located farthest from the 16B trajectory, particularly to the North (Figure 6). Condition numbers reflect sensitivity to noise in the data; thus, higher SNR signals allow stable inversions with higher condition numbers relative to lower SNR signals.

Standard deviations of the dislocation angles derived from the moment tensor solutions show that noise sensitivity is more significant on the strike and rake angles. On the other hand, dip and α angles together with M_w are more resilient (Figure 7). The angle α measures the deviation of the displacement vector from the dislocation's plane (Vavrycuk, 2011, Chapman and Leaney, 2012). Filtering the dislocation angles independently for the solutions with standard deviations below 5° and misfit below 0.4 we obtain that more than 30 events fulfill these conditions for dip and α, while for strike and rake, less than 10 events are selected. Rose plots of the filtered dip and α angles display conjugate solutions with dips around ~50° and ~80°, practically all of them corresponding with shearing or opening dislocations at angles of predominantly 30° and smaller (Figure 8).

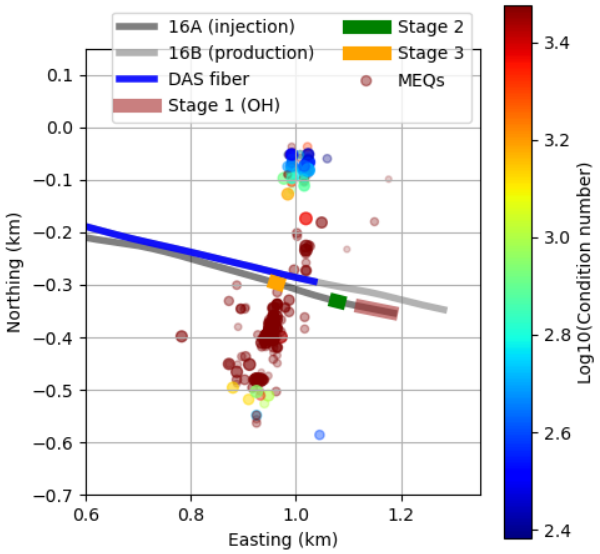

Figure 6: Distribution of condition numbers of the moment tensor inversion. Dot transparency is inversely proportional to the reliability of the location solution. Dot size is proportional to the relative magnitude of the events.

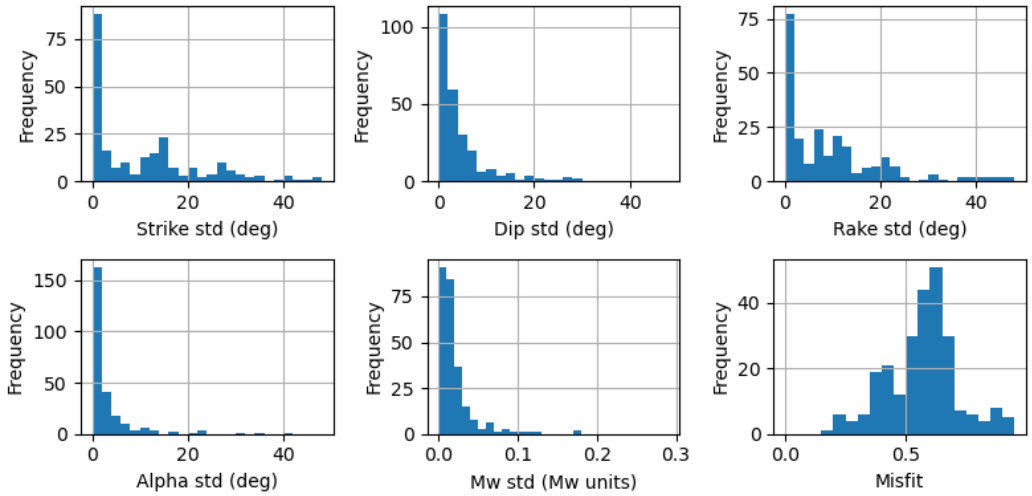

Figure 7: Distributions of standard deviations for different parameters derived from the moment tensor inversion. The bottom right panel shows the distribution of misfits for all the solutions.

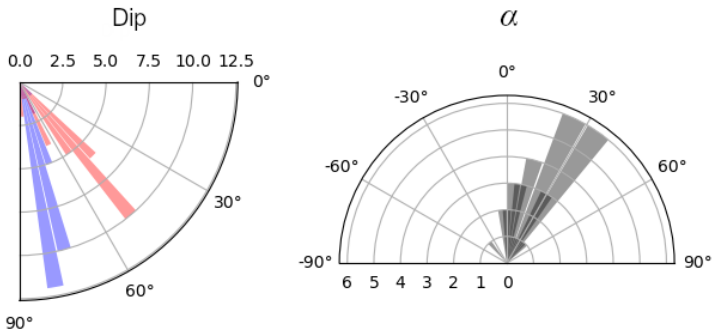

Figure 8: Rose plots of dip and α angles for solutions with standard deviation < 5° and misfit below 0.4

Figure 9 presents the pressure at the wellhead of 16A together with the angle α for the solutions with standard deviation $\sigma_\alpha < 5°$ and misfit < 0.4. If we use a conservative criterion and consider that $\alpha < 2\sigma_\alpha$ likely corresponds to pure shearing events, we have that 7 of these solutions would be double couples, one is a closing crack and the remaining 25 opening dislocations. In particular, if we consider the initial delay of 7.5 hours in seismogenic response interpreted from the rate of event detections (see Figure 3), the closing crack still coincides with a time period where wellhead pressure was dropping around 00:15 AM UTC on July 19 (the closing crack's origin time is 07:47 AM UTC). Although the opening dislocation solutions are consistent with hydraulic injection into the reservoir, the results still raise the question of why we did not observe more closing cracks at times when injection rate was decreasing. It is possible that apart from being less common, more solutions for this type of events did not pass our filtering criteria to analyze them in more detail.

Although most of the moment tensor inversion solutions showed significant sensitivity to noise in the bootstrap analysis, there is a group of 7 events for which all the dislocation angles present standard deviations under 5° and misfit < 0.4. Not surprisingly, the locations of these events fall North and South from the trajectory of well 16B in areas where condition numbers are lower (Figure 10). The solutions for 6 of these events are opening dislocations while the remaining one corresponds to the closing crack highlighted above. The geometries of the dislocations are variable although the solutions to the North repeat at least once. Referring to the numbers displayed on Figure 10, dislocation numbers 1, 3 and 5 show a similar geometry and activation style with strikes ~ [255°, 106°], dips ~ [50°, 81°] and rakes ~ [-130°, -61°], denoting normal activation consistent with their opening α ~ 35°. On the other hand, dislocations 6 and 7 present openings in a more strike-slip orientation with rakes ~ [-153°, -17°]. Their geometry form steeper planes striking ~ [44°, 284°]. A direct comparison of the DAS records for this set of dislocations North of 16B attest the differences in source radiation pattern. The most obvious difference is observed in the larger amplitudes of direct P-arrivals between channel stack numbers 400 to 600 for the more strike-slip solutions (Figure 11). The closing crack located South of 16B (i.e., dislocation 4) appears more similar to the set 1, 3, 5 in its geometry having strikes of [288°, 145°] and dips of [70°, 70°]. It's rake of activation is also similar although in reverse mode at [46°, 133°] consistent with its closing α = -35°. Dislocation 2 is an opening crack closer to strike-slip orientation in its activation with strikes [340°, 109°], dips [66°, 81°], and rakes [-26°, -145°].

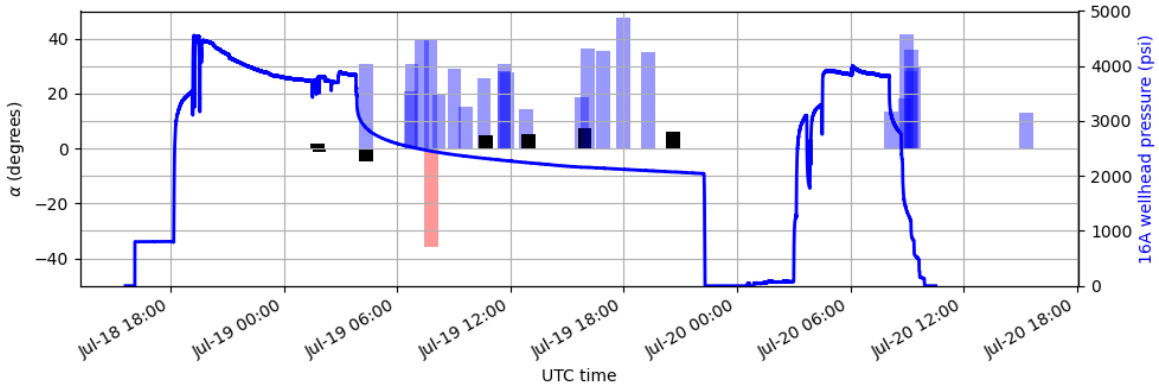

Figure 9: Dislocation angle α (left axis) as a function of time and in relation to the wellhead pressure at the injector well 16A (right axis). Blue and red bars represent opening and closing dislocations, respectively. Black bars are solutions where $\alpha < 2\sigma_\alpha$ and are considered potentially pure double-couples.

3. DISCUSSION

At first examination, none of the moment-tensor derived fracture-geometries that could be analyzed more quantitatively fit one of the four major sets described in the most recent update to the local discrete fracture network model for the FORGE site (Finnila and Jones, 2024). Nevertheless, given the variability in fracture orientations that has been described within FORGE (Jones et al., 2024), none of these solutions can be discarded. For instance, the depths of this set of events covers the range from ~700 m to ~ 880 m from MSL, which spans some of the deeper zones in the lithology classification proposed by Finnila and Jones (2024). Within these zones there are fracture sets interpreted from Formation MicroImager (FMI) and Ultrasonic Borehole Imager (UBI) logs that can be associated to one of the dislocation planes derived from the moment tensor inversion of this subset of events. For example, the dislocation solution with strike ~ 255° and dip ~ 50° for the set 1, 3, 5 can be associated to a fracture family interpreted in zone 5 at well 78B. Similarly, the dislocation solution with strike 44° and dip 83° for the set 6, 7 can also be associated with fracture sets observed in different intervals in wells 16A and 16B in both FMI and UBI logs. For the dislocation solutions in the South, there are not similar sets described in wells 16A or 16B. However, logs from vertical wells 78B and 56-32 show multiple fracture families from which it is possible to find associations at the depth interval where dislocations 2, 4 are located. In the case of dislocation 2, for the plane with strike 340° and dip 66° there exists a fracture family identified from a Conductive Lith Bound (CLB) log in zone 7 in well 56-32 with similar orientation. Similarly, the plane with strike 145° and dip 70° of the closing dislocation 4 has similar geometry to a fracture family identified in zone 5 in well 78B. Recognizing the variability in fracture families in the area and the small number of moment tensor solutions that we could analyze quantitatively, we do not consider this a strong association. However, the existence of corresponding fracture sets observed in the well logs keeps open the possibility that the observed source mechanisms are representative of the style of activation of the corresponding microseismic events.

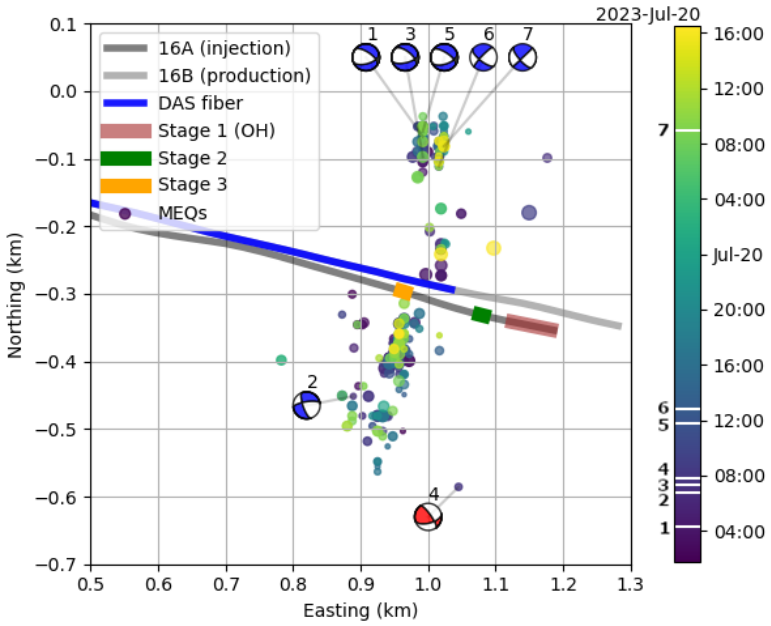

Figure 10: Beach balls for dislocation solutions with misfit < 0.4 and standard deviations < 5° in all angles. Beach balls for opening and closing solutions are colored blue and red, respectively. Numbers on top of each beach ball correspond with white lines on the color bar marking the event's origin time. The beach balls are based on one of the two dislocation planes derived from biaxial decomposition of the estimated moment tensors.

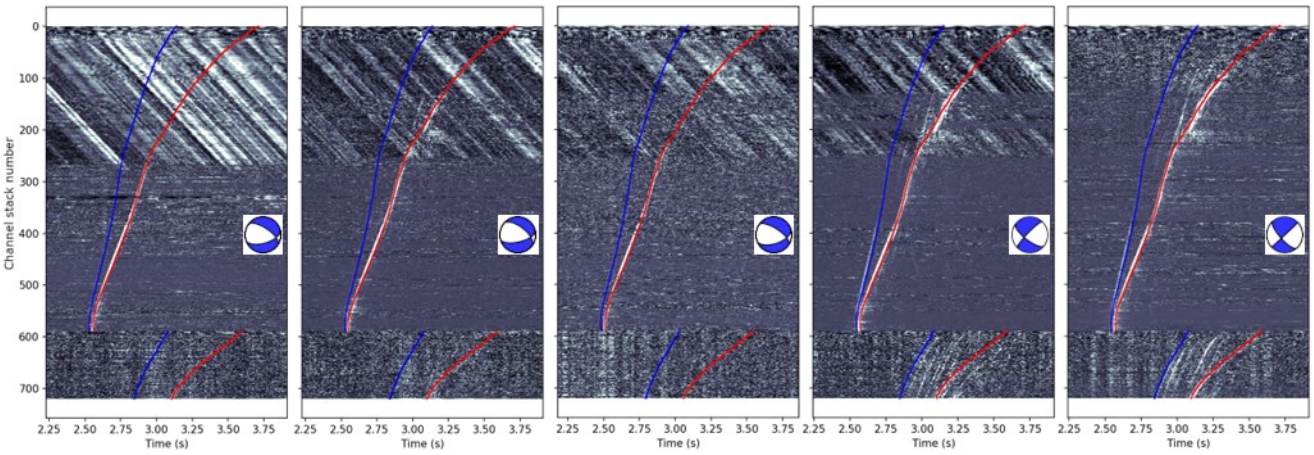

Figure 11: DAS observations for the events labeled as 1, 3, 5, 6, 7 in Figure 10, respectively. Blue and red lines highlight the direct P- and S-wave arrivals in each case.

3. CONCLUSIONS

We evaluated the constraint and solutions for the moment tensor inversion of microseismic events recorded with two DAS fibers at the Utah FORGE site. For the processing, we leveraged a new 3D velocity model calibrated with the recordings of 45 microseismic events observed at DAS systems in three different wells during stimulation work carried on in 2024. The locations of the DAS-recorded seismicity from the 2023 circulation tests were also recomputed using the new 3D model. The updated locations show better agreement with results estimated independently using data from near surface seismic stations. Condition numbers associated to the moment tensor inversion are too high near the plane that contains the trajectory of the monitoring/production well 16B, thus preventing a stable moment tensor inversion. As events are located farther from this plane, the condition numbers decrease. A bootstrap analysis of the moment tensor solutions also confirmed that sensitivity to noise decreased for events away from the plane containing 16B's trajectory.

The dislocation angles derived from biaxial decomposition of the moment tensor solutions display varying sensitivity to noise. The angles of dip and alpha (i.e., deviation of the displacement vector from the dislocation's plane) show less sensitivity with more than 30 events presenting standard deviations under 5° after the bootstrap analysis. The dips of these filtered solutions cluster in two groups, one with subvertical planes and another with more inclined solutions. Most of the α angles for these filtered events correspond to opening cracks at angles around 30° or less. This is consistent with fracture opening as a result of injection above the minimum horizontal stress. The strike and rake angles display more sensitivity to noise, and less than 10 events present standard deviations below 5° for them. A group of 7 events show low misfit under 0.4 and standard deviations under 5° for all their dislocation angles. These are located North and South from 16B's trajectory in the previously identified areas of lower condition number. In spite of being a small number to make significant interpretations, we are able to associate one of the dislocation plane solutions in each of these 7 events to fracture families previously interpreted in well logs from wells 16A, 16B and the vertical wells 78B and 56-32. This constitutes independent support to the plausibility of these solutions, although we recognize that the small set analyzed in conjunction with the high variability of fracture sets identified in well logs does not allow drawing strong conclusions.

The results from moment tensor inversions can inform future updates to the local discrete fracture network by identifying the most important fracture sets being activated by the stimulations, and thus, likely contributing to the Enhanced Geothermal System. In this respect, analysis of seismicity recorded during the more recent 2024 stimulations should yield important information as the moment tensor solutions will be constrained by at least three arrays in the case of DAS, and a dense network of surface geophones.

ACKNOWLEDGMENTS

Work carried out for research at the Utah Frontier Observatory for Research in Geothermal Energy (FORGE) was funded in part by the US Department of Energy under DE-EE0007080.

REFERENCES

Brune, J.: Tectonic stress and the spectra of seismic shear waves from earthquakes, Journal of Geophysical Research, 75, (1970), 4997-5009.

Chapman, C. and Leaney, W.: A new moment-tensor decomposition for seismic events in anisotropic media, Geophysical Journal International, 188, (2012), 343-370.

Finnila, A. and Jones, C.: Updated reference discrete fracture network model at Utah FORGE, 49th Workshop on Geothermal Reservoir Engineering, Stanford University, Proceedings (2024).

Jones, C., Simmons, S. and Moore, J.: Geology of the Utah Frontier Observatory for Research in Geothermal Energy (FORGE) Enhanced Geothermal System (EGS) site, Geothermics, 122, (2024), 103054.

Niemz, P., McLennan, J., Pankow, K., Rutledge, J. and England, K.: Circulation experiments at Utah FORGE: Near-surface seismic monitoring reveals fracture growth after shut-in, Geothermics, 119, (2024), 102947.

Shashidar, D., Vera Rodriguez, I., Mallika, K., Kuehn, D., Wilks, M., Satyanarayana, H.V.S. and Oye, V.: Relative locations of an earthquake sequence recorded during June 2017 on the Koyna-Warna borehole seismic network of western India, Bulletin of the Seismological Society of America, 110, (2020), 3130-3138.

Vavrycuk, V.: Tensile earthquakes: Theory, modeling and inversion, Journal of Geophysical Research, 116, (2011), 2011JB008770.

Vera Rodriguez, I., Stanchits, S. and Burghardt, J.: Data-driven, in situ, relative sensor calibration based on waveform fitting moment tensor inversion, Rock Mechanics and Rock Engineering, 50, (2017), 891-911.

Vera Rodriguez, I.: A heuristic-learning optimizer for elastodynamic waveform inversion in passive seismics, IEEE Transactions on Geosciences and Remote Sensing, 57, (2019), 2234-2248.

Vera Rodriguez, I. and Wuestefeld, A.: Strain microseismics: Radiation patterns, synthetics, and moment tensor resolvability with distributed acoustic sensing in isotropic media, Geophysics, 85, (2020), KS101-KS114.

Vera Rodriguez, I., Wolpert, J., Podrasky, D., Coleman, T., Maldaner, C., Ma, Y., Chamarczuk, M., Ajo-Franklin, J. and Becker, M.: DAS microseismic monitoring results from the July 2023 circulation tests at the Utah FORGE geothermal underground laboratory, SEG/AAPG International Meeting for Applied Geoscience & Energy 2024, Expanded Abstracts (2024).